Mercury's low-reflectance material: Constraints from hollows

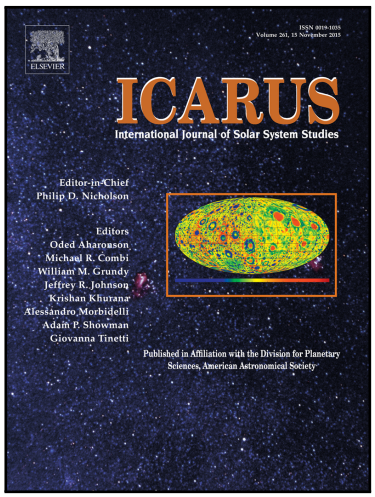

Mercury's Low-Reflectance Material: Constraints from Hollows

Rebecca J. Thomas , Brian M. Hynek , David A. Rothery , Susan J. Conway

PII: S0019-1035(16)30246-9
DOI: 10.1016/j.icarus.2016.05.036
Reference: YICAR 12084

To appear in: *Icarus*

Received date: 23 February 2016
Revised date: 9 May 2016
Accepted date: 24 May 2016

Please cite this article as: Rebecca J. Thomas , Brian M. Hynek , David A. Rothery , Susan J. Conway , Mercury's Low-Reflectance Material: Constraints from Hollows, *Icarus* (2016), doi: 10.1016/j.icarus.2016.05.036

Highlights

- We investigate the composition of Mercury's deep volatile-rich low-reflectance layer.
- Reflectance spectra of lag on sublimation hollow floors within it provide constraints.
- Analysis supports volatile (Mg,Ca) sulfides and non-volatile graphite within LRM.

Mercury's Low-Reflectance Material: Constraints from Hollows

Authors: Rebecca J. Thomas[1], Brian M. Hynek[1,2], David A. Rothery[3], Susan J. Conway[4]

[1] Laboratory for Atmospheric and Space Physics, University of Colorado, 3665 Discovery Drive, Boulder, CO 80303, USA.

[2] Department of Geological Sciences, University of Colorado, 399 UCB, Boulder, CO 80309, USA.

[3] Department of Physical Sciences, The Open University, Walton Hall, Milton Keynes, MK7 6AA, UK.

[4] Laboratoire de Planétologie et Géodynamique - UMR CNRS 6112, 2 rue de la Houssinière - BP 92208, 44322 Nantes Cedex 3, France.

Corresponding author: Rebecca J. Thomas, rebecca.thomas@lasp.colorado.edu, LASP, University of Colorado, 3665 Discovery Drive, Boulder, CO 80303, USA. Tel: +1 303 735 6065

Abstract

Unusually low reflectance material, within which depressions known as hollows appear to be actively forming by sublimation, is a major component of Mercury's surface geology. The observation that this material is exhumed from depth by large impacts has the intriguing implication that the planet's lower crust or upper mantle contains a significant volatile–rich, low–reflectance layer, the composition of which will be key for developing our understanding of Mercury's geochemical evolution and bulk composition. Hollows provide a means by which the composition of both the volatile and non–volatile components of the low–reflectance material (LRM) can be constrained, as they result from the loss of the volatile component, and any remaining lag can be expected to be formed of the non–volatile component. However, previous work has approached this by investigating the spectral character of hollows as a whole, including that of bright deposits surrounding the hollows, a unit of uncertain character. Here we use high–resolution multispectral images, obtained as the MESSENGER spacecraft approached Mercury at lower altitudes in the latter part of its mission, to investigate reflectance spectra of inactive hollow floors where sublimation appears to have ceased, and compare this to those of the bright surrounding products and the parent material. This analysis reveals that the final lag after hollow–formation has a flatter spectral slope than that of any other unit on the planet and reflectance approaching that of more space–weathered parent material. This indicates firstly that the volatile material lost has a steeper spectral slope and higher reflectance than the parent material, consistent with (Ca,Mg) sulfides, and secondly, that the low–reflectance component of LRM is non–volatile and may be graphite.

1 Introduction

The nature of unusually low reflectance material (LRM) at Mercury's surface is emerging as a key factor for understanding the planet's geochemical evolution. While initial observations of spatial variability in exposure of this material at the surface suggested a heterogeneous distribution in the subsurface [*Robinson et al.*, 2008; *Denevi et al.*, 2009], recent work suggests that it forms a deep lower crustal or upper mantle layer of global extent, brought to the surface in large impacts and then redistributed by smaller impacts [*Rivera-Valentin and Barr*, 2014; *Ernst et al.*, 2015; *Murchie et al.*, 2015]. Hence, the geological history or geochemical evolution of Mercury appears to have resulted in the formation of a distinct internal layer of unusually low reflectance material, and this requires explanation. Additionally, the observation that small, rimless depressions known as hollows form preferentially in this material, apparently primarily by sublimation [*Blewett et al.*,

2011, 2013; *Thomas et al.*, 2014], indicates that LRM not only has low reflectance, but it has a greater proportion of relatively volatile components than other surface units. This also requires explanation.

In order to explore these issues, and their implications for Mercury's evolution and composition, one must first determine the composition of LRM. Specifically, we must identify its low–reflectance component and its volatile component, and determine whether these are one and the same. Paradoxically, the solution to these global–scale questions may lie with hollows, one of Mercury's smallest–scale surface landforms. This is because hollows appear to form by the loss of the volatile component within local or regional exposures of LRM. If we can determine the composition of an LRM surface before and after hollow–formation, this should reflect a change from volatile–rich to volatile–poor, and so allow the composition of the volatile and non–volatile components to be constrained.

Attempts to identify the volatile substance(s) involved in hollow–formation using data from the MESSENGER (MErcury Surface, Space ENvironment, GEochemistry, and Ranging) spacecraft [*Solomon et al.*, 2007] have proved inconclusive [e.g., *Blewett et al.*, 2013; *Helbert et al.*, 2013]. The kilometer scale of hollows precludes detection of variations in elemental composition in and around them by MESSENGER's X–Ray Spectrometer (XRS) [*Schlemm et al.*, 2007] and Gamma–Ray and Neutron Spectrometer (GRNS) [*Goldsten et al.*, 2007], which have, at best, resolutions of hundreds of kilometers per pixel. Analyses have therefore relied on spectral reflectance data at low spectral but moderately high spatial resolution from the Mercury Dual Imaging System (MDIS) (11 bands across 433 – 1010 nm, down to < 100 m/pixel) [e.g., *Blewett et al.*, 2011, 2013; *Vilas et al.*, 2016] and at high spectral but low spatial resolution from the Visible and Infrared Spectrograph (VIRS) component of the Mercury Atmospheric and Surface Composition Spectrometer (MASCS) (5–nm resolution across 300 – 1450 nm, footprint size ≥ 0.1 km cross–track and 3 km along–track) [*Izenberg et al.*, 2015]. However, the relatively featureless character of Mercury's surface spectra presents an obstacle to direct determination of composition: absorption bands used to determine mineralogy on other planetary surfaces and in terrestrial laboratory experiments are weakly developed even in fresh material due to a low abundance of ferrous iron [*Hapke et al.*, 1975; *Vilas*, 1985; *Warell*, 2003; *Izenberg et al.*, 2014], and are further weakened by rapid optical maturation in the high–energy space environment at Mercury [*Lucey and Riner*, 2011; *Riner and Lucey*, 2012]. Studies have therefore focused on broad spectral characteristics, in particular spectral slope and overall reflectance across the visible to near–infrared spectrum, which vary for different units on

Mercury's surface (Figure 1). This has revealed that the bright material in and around hollows (referred to in this paper as BCFD, Bright Crater Floor Deposit, for convenience and for historical reasons [*Robinson et al.*, 2008], though it should be noted that these are not always on crater floors) has a flatter spectral slope (is 'bluer') across the visible spectrum than any other surface unit and is more reflective (is 'brighter') than any unit barring fresh ejecta [*Blewett et al.*, 2009]. The LRM within which hollows commonly form has a flatter spectral slope than all other units barring BCFDs, but has the lowest reflectance across the visible spectrum of the recognized regional unit types [*Murchie et al.*, 2015]. On this basis, it has been suggested that hollow–formation involves the loss of the 'darkening' agent within LRM [*Blewett et al.*, 2013], which may be spectrally neutral (making LRM relatively 'blue' by counteracting the 'redness' of other components) [*Blewett et al.*, 2009]. Calcium or magnesium sulfides are most commonly–cited as candidates for the relatively volatile substance [*Blewett et al.*, 2011, 2013; *Helbert et al.*, 2012], on the basis of the high concentration of sulfur detected at Mercury's surface [*Nittler et al.*, 2011; *Evans et al.*, 2012], expectations for mineralogy under Mercury's highly reducing conditions [*Burbine et al.*, 2002], and correlations between sulfur, calcium and magnesium abundance in heavily–cratered terrains [*Weider et al.*, 2015]. This hypothesis has recently gained further support from observations of anomalously high exospheric calcium above the extensively–hollowed Tyagaraja crater [*Bennett et al.*, 2016]. Laboratory experiments with magnesium, calcium and manganese sulfides do indicate that sulfides can be volatilized at the daytime temperatures experienced at Mercury's surface, and that extreme thermal cycling on the planet's surface could account for the lack of characteristic absorption bands [*Helbert et al.*, 2012, 2013], but have not provided a spectral match to BCFDs, LRM, or indeed any surface unit on Mercury [*Blewett et al.*, 2013; *Izenberg et al.*, 2014].

A major issue with the above approaches, however, is that the nature of BCFDs is uncertain. The spectra and localization of this material prompted *Blewett et al.* [2013] to suggest a number of possible hypotheses for its formation: chemical alteration, vapor–deposited coatings, partial removal of the darkening agent in LRM, and/or an anomalous texture. It has not yet been possible to establish which, if any, of these hypotheses is correct. Moreover, the use of BCFDs to characterize compositional changes to form hollows presupposes that they reflect an end–product of hollow–formation. However, the highest resolution Mercury Dual Imaging System (MDIS) Narrow Angle Camera (NAC) [*Hawkins et al.*, 2009] images obtained by MESSENGER suggest that this is not a valid assumption. These images show that BCFDs occur in halos around and on surviving knobs of material within hollows, indicating that they form at the active front of hollow–formation, in contrast to lower–reflectance flat hollow floors, where material loss appears to have ceased (Figure

2). This suggests that, while BCFDs are an intermediate product of unknown character, hollow floor material represents the volatile–depleted end–result of hollow–formation, and may provide the key to distinguishing the volatile and non–volatile component of the parent material. Fortunately, as MESSENGER approached Mercury at lower altitudes during the latter part of its mission, it obtained multispectral images at sufficiently small pixel sizes to discriminate flat hollow floors from BCFDs. Here, we use multispectral data to compare the spectral character of BCFD halos, high–reflectance hollow floor knobs, flat hollow floors and parent material to characterize changes in texture and composition during hollow–formation. These comparisons allow us to investigate physical and composition changes over the course of hollow–formation, and thus provide constraints on the composition of parental LRM.

2 Methods of analysis

2.1 Spectral analysis

To identify sites where a spectral analysis of hollow–related units is feasible, we first identified all hollows globally. The methods used are described in *Thomas et al.* [2014], and we have since used the same methods to expand the catalogue published therein on the basis of all MESSENGER MDIS images with a resolution of 180 m/pixel or better released up to October 2015.

We identified ten hollow groups where MDIS NAC images (which have a single medium–band filter centered on 750 nm) show parts of the hollow floor to be flat (lacking knobs of material) and for which MDIS Wide–Angle Camera (WAC) multispectral images are available with a pixel size smaller than that of the flat hollow floor area (Table 1). Multispectral images were obtained by the WAC by rotation of a 12–position filter wheel to different positions for successive images. This resulted in sets of largely overlapping images taken under similar lighting and spacecraft pointing conditions but capturing different parts of the spectrum. We selected the best resolution set of WAC images with an intermediate phase angle (see Section 2.2) available for each site, and radiometrically and photometrically corrected and coregistered the 430 nm and 750 nm images using the ISIS3 image processing package of the USGS. We calculated spectral slope (VISr, the ratio of reflectance at 430 nm to that at 750 nm) by division of one image by the other. This measure of visible spectral slope is comparable with that used for VISr in MASCS data by *Izenberg et al.* (2014, 2015) (415 nm / 750 nm) (Figure 1). We coregistered higher–resolution NAC images with the WAC data, and used these to identify regions that correspond to the specific unit types listed in Table 2 (Figure 3). Multiple

samples of each unit type were selected for each site, and the mean, minimum and maximum values for VISr and reflectance at 750 nm (R750) were extracted for each sample (Figure SF1).

Previous work on reflectance spectra from the VIRS component of MASCS indicates that spectral slope in the UV range at hollow sites is generally similar to that of surrounding substrates, raising a number of hypotheses regarding their composition and/or the correct interpretation of the spectral data [*Izenberg et al.*, 2014, 2015]. However, as the aforementioned studies did not discriminate between BCFDs and hollow floors, these findings may correspond to a mixed spectrum of the two unit types. In most cases, the footprint size of MASCS (which is, at best, 0.1 km cross–track and 3 km along–track) is insufficient to discriminate hollow floors. However at two of the selected sites, Eminescu and Raditladi craters, flat hollow floors are of broad enough spatial extent to potentially be characterized by the detected spectrum. Because MASCS is non–imaging, it is possible that MASCS footprints have been incorrectly coregistered with respect to MDIS data (global monochrome mosaic). Therefore, we obtained calibrated spectral reflectance MASCS data from the Planetary Data System (PDS) for along–track footprints crossing an area of hollows rather than analyzing individual footprints that appear to be co-located with hollow floors. This approach has the added virtue of comparing spectra acquired along a specific orbit, thus removing the potential for variation due to viewing conditions. Using these data, we examined how spectral slope in the UV range (UVr, 310 nm / 390 nm, Figure 1) varies with R750 and VISr across hollows, BCFDs and parental units.

Though Mercury spectra, including those around hollows [*Izenberg et al.*, 2014] have in general been found to lack spectral absorptions indicating specific mineralogy, at some hollow sites intriguing indications of spectral absorption around 600 nm have been reported [*Vilas et al.*, 2016], which may indicate the presence of sulfides [*Vilas et al.*, 2016], graphite or nanophase and microphase iron [*Murchie et al.*, 2015]. At sites where WAC observations over the eight most commonly–used WAC filters (430,480, 560, 630, 750, 830, 900 and 1000 nm) have been made at sufficient spatial resolution to discriminate hollow floors (Group 4030, Eminescu crater and Raditladi basin), we constructed coregistered composites using all 8 bands and took mean reflectance values at each wavelength for the example regions previously used to explore the VISr and R750 of each unit type. We used these to construct spectra in which such an absorption could potentially be detectable. The MASCS data described above were also scrutinized for absorption bands, but none were observed.

2.2 Photometric effects

The phase angle (the angle between direction of solar incidence and direction of viewing) at which the surface of an atmosphere-less body is viewed affects the detected spectral reflectance. This is because inter– and intra–particle roughness casts larger shadows at larger phase angles, leading in general to lower reflectance at higher phase angles [*Hapke*, 2002]. We therefore utilized WAC observations with as narrow a range of phase angles as possible (Table 1), and considered to what extent such variations in phase angle could account for observed variations in dynamic range (variation in absolute reflectance) between sites.

Further, because surfaces dominated by coarser–grained or rougher materials cast longer shadows at the same phase angle than smoother or finer–grained surfaces, the magnitude of this response can be used to infer the structural properties of a surface [*Kaydash et al.*, 2012]. This effect has been utilized to study the dominant grain size of BCFDs by creating phase–ratio images by dividing reflectance values of a lower phase angle image by those of a coregistered higher phase angle image [*Blewett et al.*, 2014]. Here we have applied this method by selecting, where available, two high–resolution NAC images for each site with a similar spatial footprint and resolution but a phase angle differing by at least 20°. We calibrated these images to I/F, coregistered them using ArcGIS software and created a phase ratio image by dividing reflectance values in the image with a greater phase angle by those of that with a lesser phase angle ($R(\alpha1)/R(\alpha2)$ where $\alpha1 > \alpha2$) . This ratio (the inverse of that used by *Blewett et al.*, [2014]) was used because it allows the additional effect of albedo to be more readily visually assessed in the phase ratio image. At the intermediate phase angles of the images used for this analysis, $R(\alpha1)/R(\alpha2)$($\alpha1 > \alpha2$) correlates directly with $R(\alpha2)$ as a result of multiple light scattering within and between particles [*Kaydash et al.*, 2012]. Hence units with relatively high reflectance at lower phase angles, such as BCFDs and hollow floors, can be expected to have a higher phase ratio than other substrates as a result of their albedo, even if their surface roughness or grain size does not differ from that of those other units. If, on the contrary, they do not have a higher $R(\alpha1)/R(\alpha2)$($\alpha1 > \alpha2$) phase ratio, this cannot be explained by albedo and must result from distinct structural properties. Because topography also affects phase angle, phase ratio comparison was made only between large (>50 pixels), uniform samples of each unit, and all scarps and shadowed areas were excluded from the analysis. The mean phase ratio of samples of each unit type was calculated for each site.

3 Results: Spectral variation at hollow sites

On the basis of MDIS images released between March 2014 and October 2015, we identified 163 sites where hollows occur in addition to those catalogued in *Thomas et al.* [2014], bringing the number of sites where hollows have been identified on Mercury to 608 (Supplementary Table TS1). The association of hollows with local or regional LRM remains at the previously–reported level of 96% of the global hollowed area. As in the earlier version of the catalogue, only 7% and 8% of the hollowed area occurs in the smooth plains types HRP and LBP, respectively, and even those examples have nearby localized occurrences of LRM visible in 85% and 68% of those cases.

The relative spectral attributes of the different units, as derived from MDIS multispectral data, are broadly consistent across the ten sites analyzed (Figure 4). They are particularly well–characterized where there are large areas of flat hollow floor, as at Eminescu crater (Figure 5). Flat hollow floors have the lowest spectral slopes of the unit types (they are relatively blue, having high VISr), followed by BCFDs and partially–developed hollows. BCFDs and partially–developed hollows reach the highest values of R750, though the mean value within each analyzed sample area overlaps with that of hollow floor samples. This is to be expected even if BCFDs have higher R750 than hollow floors, because BCFD halos have diffuse margins, leading to spectral mixing with lower R750 substrates where they thin, and partially–developed hollows are expected to contain a spectral mix of BCFDs and sub–pixel–scale flat hollow floor. Hollow floors R750 ranges down to that of non-LRM unhollowed units in Eminescu crater and 8006.

The absolute range in VISr and R750 values differs between sites, particularly in Pasch crater and Raditladi basin, where hollow floors with very low spectral slope and BCFDs with very high-reflectance values are observed. A greater dynamic range is expected at high phase angles due to the different responses of surfaces with different structural properties, and this factor can account for some of the variability. When Pasch and Raditladi are excluded, R750 and the phase angle of the WAC observation show a moderate to strong correlation, demonstrated by a Pearson's product-moment correlation of 0.68, where 1 is total positive correlation, and a 7% possibility that this correlation arises by chance. The divergence of spectra at Pasch and Raditladi from this trend indicates that other factors, photometric or physical, may be responsible for their high dynamic range. We observe no shift to steeper spectral slopes with higher phase angle (phase reddening), as seen on other atmosphere-less bodies [e.g., *Lane and Irvine*, 1973; *Sanchez et al.*, 2012]: indeed, sites with the lowest detected spectral slopes (Pasch crater, Raditladi basin and Group 8006) were

observed at relatively high phase angles. This lack of phase reddening is consistent with global analysis of MDIS data by *Domingue et al.* [2011], but *contra* that of *Murchie et al.* [2015].

Phase ratio images derived from NAC images give consistent results across all sites (e.g. Figure 6). BCFD halos and partially-developed hollows show an above-average phase ratio, as reported previously [*Blewett et al.*, 2014]. However, as discussed in Section 2, the high intrinsic albedo, rather than the physical properties of the material, could potentially produce this result. Conversely, hollow floors, which, like BCFDs, have high albedo in moderate phase angle images, have a phase ratio similar to or lower than that of surrounding crater floor and LRM units. This phase ratio is lower than would be expected to result from albedo, and indicates that they have a high surface roughness and/or are coarse–grained. Where there are large expanses of hollow floor, the phase ratio is lowest away from the walls, indicating that material with these physical properties is in situ floor material rather than material mass wasted from the walls.

Of the three sites where an 8–filter range of multispectral WAC images is available for analysis, a band absorption around 600 nm is seen only at Raditladi (Figure 7). Here, all hollow floor spectra have a broad absorption between 430 and 820, centered near 600 nm. The two brightest BCFD halos and, to a less degree, a dimmer BCFD halo and all partially–hollowed areas have spectra indicating a more localized absorption at 630 nm. These absorptions remain after normalizing to the reflectance spectrum of the wider crater floor.

In MASCS footprints from Eminescu with high VISr and R750 that appear to be located in areas with hollow floor or hollow floor combined with BCFD, UVr is near the planetary average (which is 0.65–0.71 [*Izenberg et al.*, 2014]) and similar to that of the wider crater floor, whereas the LRM immediately surrounding the hollowed area has very low UVr, similar to that observed in pyroclastic deposits and bright ejecta [*Izenberg et al.*, 2014] (Figure 5c, Figure 8a). In Raditladi, all UVr values are unusually low. The UVr of footprints that VISr, R750 and spacecraft tracking information indicate coincide with hollow floors is similar to that of footprints that appear to detect LRM mixed with BCFD (Figure9a, Figure 10). At both sites, footprints interpreted as BCFD on the basis of high R750 and moderate VISr have slightly lower UVr than hollow floors.

The low UVr of all MASCS observations at Raditladi and the anomalously low UVr of LRM at both Eminescu and Raditladi compared to global values of ≥7.1 [*Izenberg et al.*, 2014] could indicate that these two sites have anomalous composition, texture or maturity. We therefore additionally calculated R750, VISr and UVr for MASCS footprints along tracks crossing hollows in Seuss crater

(Group 5001), Kertesz crater (Group 6070), Group 8001, an additional two tracks each at Eminescu and Raditladi, and across two areas where LRM is present but there is no evidence of hollows, the ejecta blankets of Tolstoj and Nabokov crater (Table ST2). We used the highest-resolution MASCS observations available in order to maximize detection of spectral variability. Though the spatial resolution is not sufficient to capture an unmixed hollow floor spectrum, they provide UVr for mixed hollow floor/BCFD/LRM spectra, and unmixed crater floor material and LRM.

We find that, if data from tracks crossing the northeast peak ring of Raditladi basin and hollows north of the central peak of Eminescu crater are excluded, the UVr of footprints containing BCFD and hollow floors ranges from similar to, to somewhat higher than, that of crater floor material and LRM, close to the average for Mercury materials (0.65-0.70 [*Izenberg et al.*, 2014]) (Figure SF2). UVr of hollows-proximal LRM is lower than previously-reported values of ≥7.1 (Figure SF3), but lies within the range we observe for non-hollowed LRM at Tolstoj and Nabokov. Anomalously low (0.58) UVr LRM at Eminescu is seen only in the track within which a hollow floor spectrum can be detected (Eminescu 1, Figure 8a); LRM UVr in footprints from nearby tracks is, as at other analyzed hollowed sites, 0.6-0.65 (Figure 8b,c). We therefore interpret the hollow floor and BCFD UVr detected in Eminescu 1 as slightly above that of parental LRM materials. All Raditladi UVr detections in the two tracks crossing the NE peak ring (Raditladi 1 and 2) are anomalously low, unlike those from Raditladi 3, crossing the NE peak ring (Figure 9, Figure 10). We therefore interpret hollow floor and BCFD spectra for Raditladi 1 as similar to that of the parental material.

4 Discussion

4.1 Interpretation of the spectral evidence

Our results imply that flat, apparently inactive floors within hollows have a lower spectral slope at visible wavelengths and lower reflectance than the bright material present during hollow formation. Both units have higher reflectance and a lower spectral slope at visible wavelengths than surrounding units, which presumably contain material yet to be lost by hollow–forming process(es). UV spectral slope of both BCFDs and hollow floors is similar to slightly higher than that of parental material. Spectral character in these broad terms is primarily controlled by maturity, composition and texture (e.g. grain size). Consideration of these factors suggests two possible explanations for the observations.

4.1.1 Maturity: Hollows uncover immature exposures of their parental material

Hollow floors may simply represent less space weathered examples of their parent material. Under the high flux and high velocity micrometeoroid bombardment at Mercury's surface, any exposed surface is quickly darkened and reddened by the condensation of very fine–grained iron coatings onto mineral grains, and further darkened by the aggregation of these coatings within agglutinate glasses to form slightly larger sub–microscopic iron particles [*Lucey and Riner*, 2011; *Riner and Lucey*, 2012]. This means that any freshly–exposed surface is expected to have relatively high reflectance and a flatter reflectance spectrum than older surfaces (it will be relatively bright and 'blue'). Thus, a fresh surface could be expected to have the characteristics in the visible spectrum observed for hollow floors, and this could also explain the observation that the UV spectral slope of hollow floors at Raditladi is similar to that of the parent material, as observed elsewhere [*Izenberg et al.*, 2015]. If the spectrum of hollow floors is the result of immaturity alone, it cannot be used to identify the volatile substance(s) lost in hollow formation.

However, this hypothesis is inconsistent with the evidence presented here on three counts:

1. Spectral slope relative to BCFDs: The occurrence of BCFD preferentially around hollows and on upstanding knobs within them suggests that BCFD occurs where hollow-forming processes are active, and that this activity has ceased on flat hollow floors. If this interpretation is correct, hollow floors have been exposed to space weathering for longer than BCFD and so their spectral slope should either be steeper [*Hapke*, 2001] or unchanged [*Lucey and Riner*, 2011]. Instead, it is flatter.
2. Response of UV spectral slope to maturity: Spectral slope at UV wavelengths is also inconsistent with that of immature parent material. Spectral studies of asteroids and laboratory and remote sensing data for lunar mare soil indicate that space weathering decreases UV spectral slope, particularly in the 300–400 nm range [*Hendrix and Vilas*, 2006]. This means more space weathered materials will have higher UVr, and yet our observations indicate that hollow floors and BCFDs have similar or higher UVr than more mature parental LRM. UVr is also affected by composition and texture: both higher transition metal content and, in basalts, larger grain size result in lower reflectance and higher UVr [*Cloutis et al.*, 2008]. The phase ratio results presented here support the presence of coarser–grained or rougher material on hollow floors than in BCFDs, potentially accounting for the higher UVr for hollow floors versus BCFDs in Eminescu and Raditladi. This factor could also account for the below-average UVr of hollow-proximal LRM (and

particularly that at Raditladi and Eminescu) if exposed LRM retaining its volatile component has an above-average proportion of fine-grained material. Compositional differences, in particular the concentration of non–volatile transition metal bearing minerals in a lag, may also contribute to the higher UVr of hollow floors versus BCFDs and of average versus non-volatile-depleted LRM.

3. Morphology: For fresh parental material to be exposed at hollow floors, accumulation of lag must be slight. However, in the absence of a lag, hollow–formation should continue until all volatile material is lost. There is no evidence that hollows form within a thin volatile–bearing stratum of consistent thickness, and yet hollow floors are flat, and hollows have a characteristic depth of several tens of meters across the planet [*Blewett et al.*, 2011; *Vaughan et al.*, 2012; *Thomas et al.*, 2014]. If we instead propose that a relatively volatile substance percolated through the parent material, the loss of this substance could leave a hole floored by parent material that has been churned but not otherwise affected. In that case, however, the morphology of hollows would be expected to indicate subsidence rather than scarp retreat. Such a process may be applicable to pitted ground seen elsewhere on the planet [*Thomas et al.*, 2014], where the loss of hollow–forming volatiles does create a morphology indicative of subsidence, but it is not a good model for hollow–formation.

4.1.2 Composition: Hollows are floored by the non–volatile component of the parent material

Given the morphology of hollows, the most probable model for their formation is that proposed by *Blewett et al.* (2013), in which a high proportion of the parent material is volatilized to form hollows, leaving behind a lag that ultimately prevents further deepening, while the high–relief hollow margins continue to recede, widening the hollow. The observed spectral slope of hollow floors fits well with this model: if partial loss of volatiles during hollow–formation leads to a relatively 'blue' spectral character for BCFDs, the even 'bluer' hollow floors represent a greater degree of (or total) removal. This indicates that the relatively volatile substance(s) lost in hollow–formation is relatively red–sloped. Evidence for the reflectance of the substance(s) lost is less certain: though the lower reflectance commonly seen in hollow floors versus BCFDs and partially–developed hollows could result from a greater fractional loss of a substance with relatively high reflectance, it could equally result from the greater maturity of hollow floors. Nevertheless, their relatively low reflectance is not consistent with the hypothesis that the loss of the volatile substance(s) has a 'brightening' effect [*Blewett et al.*, 2013]. Indeed, as hollow floors are relatively young, they would be expected to be brighter than surrounding older units even if they result from

the loss of a higher–reflectance substance within those surrounding units (though we note that the rate of optical maturation on Mercury is not yet well–constrained). Thus, volatile–loss either has little effect or a darkening effect on the reflectance of the parent material, suggesting that the substance responsible for the low reflectance of LRM is non–volatile.

The results and interpretation of the phase-ratio analysis reported here allow us to gain a more complete understanding of the texture of hollows. *Blewett et al.* [2014] grouped hollow floors and bright haloes together in their phase-ratio study of one hollows location (Eminescu). On the basis of the results of a correlation test (as used by *Shkuratov et al.* [2012]) they argued that the low absolute reflectance of Mercury materials results in little multiple scattering, and hence that change in brightness with phase angle can be attributed to sub-resolution texture or particle scattering properties rather than albedo. This led them to conclude that the phase behavior of the hollows (floors + BCFD haloes) was consistent with the presence of finer particle sizes than in the background regolith.

Here we carried out more detailed work for 8 hollows sites, by treating the floors and bright haloes separately. We agree that the BCFDs show phase behavior that is consistent with fine particles, given that albedo does not in fact play a role. But our key finding concerns the nature of the lag on the floor of the hollows. The response to phase angle observed in the final lag, which lies on the flat floors of hollows, indicates that it is coarse–grained or rougher in texture relative to BCFDs and usually also relative to parental material. This may result from the intrinsic morphology of minerals in the residuum (e.g., coarse, angular crystals) or from breakup along widely–spaced planes, as a result of concentration of the volatile component along such planes.

4.2 Implications for the nature of Mercury's low–reflectance material

The above indicates that LRM in which hollows form contains a volatile component with a relatively high reflectance and steep spectral slope, and a separate non–volatile component that has low reflectance and a flatter spectral slope. This confirms that (Ca,Mg) sulfides subjected to Mercury's extreme diurnal thermal cycle, which are spectrally consistent with the former, are good candidates for the volatile substances responsible for hollow–formation [*Burbine et al.*, 2002; *Helbert et al.*, 2012; *Blewett et al.*, 2013]. Additionally, it supports the hypothesis that graphite (a low–reflectance, opaque mineral) is a darkening agent on Mercury [*Murchie et al.*, 2015], which has recently received major support by thermal neutron measurements indicating an enhancement in carbon of 1–3 wt% at major exposures of LRM [*Peplowski et al.*, 2016]. This is intriguing in light of the twin

hypotheses that graphite makes up Mercury's primary flotation crust [*Vander Kaaden and McCubbin*, 2015] (perhaps above a sulfide lid [*Parman et al.*, 2016]) and that LRM is exhumed from the lower crust [*Rivera-Valentin and Barr*, 2014; *Ernst et al.*, 2015] from beneath later effusive volcanic deposits [*Whitten et al.*, 2014].

It is tempting to take the 8–filter MDIS data from Raditladi as further confirmation of this: the narrower absorption at 560 nm is consistent with that expected for (Ca,Mg) sulfides (and is consistent with absorptions observed in hollowed regions of Dominici crater [*Vilas et al.*, 2016]), while the broader absorption around 600 nm in hollow floor spectra is consistent with that of graphite [*Murchie et al.*, 2015]. This could be interpreted as showing still–present sulfides where hollow–formation is ongoing, and their lack and a stronger spectral effect from the remaining graphite in hollow floors when no further sulfides are present at the surface. However, due to the low spectral resolution of MDIS, and the lack of observed absorption features in 8–filter MDIS data from Eminescu or site 4030, or in higher–spectral resolution MASCS data for Raditladi, Eminescu or Kertesz, we are wary of placing any great weight on this result.

5 Conclusions

Spectral analysis of the floors of Mercury's hollows indicates that they form by loss of a relatively bright and red–sloped volatile component, leaving behind a relatively rough or coarse–grained lag with a flatter (bluer) spectral slope and, potentially, the same or lower reflectance than the parent material. As this parent material is most commonly the globally–occurring low–reflectance substrate, LRM, this substantiates suggestions that the volatile substance(s) within LRM are sulfides, and indicates that its darkening component is non–volatile and could be graphite.

Because this analysis depends on data from a small number of sites (ten), it is possible that hollow floors display a greater range in spectral character than represented by this sample. Fortunately, the instrumental capabilities of the forthcoming BepiColombo mission are ideally suited to the measurement of surface spectra at a spatial resolution necessary to discriminate hollow floors: the visible and near–infrared component of its SIMBIO–SYS (VIHI) [*Flamini et al.*, 2010] and the MERTIS thermal–infrared spectrometer [*Hiesinger and Helbert*, 2010] cover a spectral range of 400–2000 nm and 7–14 μm, respectively, and will obtain global data at 500 m/pixel or better (up to 100 m/pixel for targeted VIHI observations). As both MERTIS and VIHI are imaging it will also be easier to correlate morphological features with spectral data than it is with MASCS. The STC component of SYMBIO–SYS will provide additional global data at much better spatial resolutions

(50 m/pixel), though at lower spectral resolution. Its 420 nm and 700 nm filters are broadly comparable to the 430 nm and 750 nm MDIS filters used to analyze spectral slope here. Finally, the radiometric component of MERTIS, with its ability to constrain thermal inertia, will be invaluable for separating the effect of physical properties from that of composition on remotely–sensed reflectance spectra. With the help of these data, it will be possible to analyze compositional and textural trends during hollow–formation at a greater number of sites, and perhaps to come to a better understanding of the precise nature of BCFDs.

Acknowledgements

This research was conducted with support from NASA (Planetary Geology and Geophysics grant NNX14AP51G), the Science and Technology Facilities Council (UK) (grants ST/K502212/1 and ST/L000776/1), and the UK Space Agency (grants PP/E002412/1 and ST/M002101/1). All MESSENGER images are credited to NASA/Johns Hopkins University Applied Physics Laboratory/Carnegie Institution of Washington. Our thanks to Dr. Mikki Osterloo at the Laboratory for Atmospheric and Space Physics, Boulder, Colorado for her helpful feedback on the manuscript, and to Dr. David Blewett and an anonymous reviewer for their thoughtful and constructive reviews.

References

Bennett, C. J., J. L. McLain, M. Sarantos, R. D. Gann, A. DeSimone, and T. M. Orlando (2016), Investigating potential sources of Mercury's exospheric calcium: Photon-stimulated desorption of calcium sulfide, *J. Geophys. Res. Planets*, doi:10.1002/2015JE004966.

Blewett, D. T., M. S. Robinson, B. W. Denevi, J. J. Gillis-Davis, J. W. Head, S. C. Solomon, G. M. Holsclaw, and W. E. McClintock (2009), Multispectral images of Mercury from the first MESSENGER flyby: Analysis of global and regional color trends, *Earth Planet. Sci. Lett.*, *285*(3-4), 272–282, doi:10.1016/j.epsl.2009.02.021.

Blewett, D. T. et al. (2011), Hollows on Mercury: MESSENGER evidence for geologically recent volatile-related activity., *Science (80-.).*, *333*(6051), 1856–1859, doi:10.1126/science.1211681.

Blewett, D. T. et al. (2013), Mercury's hollows: Constraints on formation and composition from analysis of geological setting and spectral reflectance, *J. Geophys. Res. Planets*, *118*(5), 1013–1032, doi:10.1029/2012JE004174.

Blewett, D. T., C. L. Levy, N. L. Chabot, B. W. Denevi, C. M. Ernst, and S. L. Murchie (2014), Phase-ratio images of the surface of Mercury: Evidence for differences in sub-resolution texture, *Icarus*, *242*, 142–148, doi:10.1016/j.icarus.2014.08.024.

Burbine, T. H., T. J. Mccoy, L. R. Nittler, G. K. Benedix, E. A. Cloutis, and T. L. Dickinson (2002), Spectra of extremely reduced assemblages: Implications for Mercury, *Meteorics Planet. Sci.*, *37*, 1233–1244.

Cloutis, E. A., K. A. McCormack, J. F. Bell, A. R. Hendrix, D. T. Bailey, M. A. Craig, S. A. Mertzman, M. S. Robinson, and M. A. Riner (2008), Ultraviolet spectral reflectance properties of common planetary minerals, *Icarus*, *197*(1), 321–347, doi:10.1016/j.icarus.2008.04.018.

Denevi, B. W. et al. (2009), The evolution of Mercury's crust: a global perspective from MESSENGER., *Science*, *324*(5927), 613–618, doi:10.1126/science.1172226.

Domingue, D. L., S. L. Murchie, N. L. Chabot, B. W. Denevi, and F. Vilas (2011), Mercury's spectrophotometric properties: Update from the Mercury Dual Imaging System observations during the third MESSENGER flyby, *Planet. Space Sci.*, *59*(15), 1853–1872, doi:10.1016/j.pss.2011.04.012.

Ernst, C. M. et al. (2015), Stratigraphy of the Caloris Basin: Implications for volcanic history and basin impact melt, *Icarus*, *250*, 413–429, doi:10.1016/j.icarus.2014.11.003.

Evans, L. G. et al. (2012), Major-element abundances on the surface of Mercury: Results from the MESSENGER Gamma-Ray Spectrometer, *J. Geophys. Res.*, *117*, E00L07, doi:10.1029/2012JE004178.

Flamini, E. et al. (2010), SIMBIO-SYS: The spectrometer and imagers integrated observatory system for the BepiColombo planetary orbiter, *Planet. Space Sci.*, *58*(1-2), 125–143, doi:10.1016/j.pss.2009.06.017.

Goldsten, J. O. et al. (2007), The MESSENGER Gamma-Ray and Neutron Spectrometer, *Space Sci. Rev.*, *131*(1-4), 339–391, doi:10.1007/s11214-007-9262-7.

Hapke, B. (2001), Space weathering from Mercury to the asteroid belt, *Geology*, *106*, 39–73, doi:10.1029/2000JE001338.

Hapke, B. (2002), Bidirectional reflectance spectroscopy: 5. The coherent backscatter opposition

effect and anisotropic scattering, *Icarus*, *157*, 523–534, doi:10.1006/icar.2002.6853.

Hapke, B., G. E. Danielson, K. Klaasen, and L. Wilson (1975), Photometric observations of Mercury from Mariner 10, *J. Geophys. Res.*, *80*(17), 2431–2443, doi:10.1029/JB080i017p02431.

Hawkins, S. E. et al. (2009), In-Flight Performance of MESSENGER's Mercury Dual Imaging System, *Proc. SPIE, Int. Soc. Opt. Eng.*, *SPIE7441*, doi:10.1117/12.826370.

Helbert, J., A. Maturilli, W. M. Vaughan, J. W. Head, R. L. Klima, T. David, and T. J. McCoy (2012), Spectral Reflectance Measurements of Sulfides at the Planetary Emissivity Laboratory — Analogs for Hollow-Forming Material on Mercury?, *Lunar Planet. Sci. Conf.*, *43*, 1381.

Helbert, J., A. Maturilli, and M. D'Amore (2013), Visible and near-infrared reflectance spectra of thermally processed synthetic sulfides as a potential analog for the hollow forming materials on Mercury, *Earth Planet. Sci. Lett.*, *369-370*, 233–238, doi:10.1016/j.epsl.2013.03.045.

Hendrix, A. R., and F. Vilas (2006), The effects of space weathering at UV wavelengths: S-Class asteroids, *Astron. J.*, *132*(3), 1396–1404, doi:10.1086/506426.

Hiesinger, H., and J. Helbert (2010), The Mercury Radiometer and Thermal Infrared Spectrometer (MERTIS) for the BepiColombo mission, *Planet. Space Sci.*, *58*(1-2), 144–165, doi:10.1016/j.pss.2008.09.019.

Izenberg, N. R. et al. (2014), The low-iron, reduced surface of Mercury as seen in spectral reflectance by MESSENGER, *Icarus*, *228*, 364–374, doi:10.1016/j.icarus.2013.10.023.

Izenberg, N. R., R. J. Thomas, D. T. Blewett, and L. R. Nittler (2015), Are there compositionally different types of hollows on Mercury?, *Lunar Planet. Sci. Conf.*, *46*, 1344.

Vander Kaaden, K. E., and F. M. McCubbin (2015), Exotic crust formation on Mercury: consequences of a shallow, FeO-poor mantle, *J. Geophys. Res. Planets*, doi:10.1002/2014JE004733.

Kaydash, V., Y. Shkuratov, and G. Videen (2012), Phase-ratio imagery as a planetary remote-sensing tool, *J. Quant. Spectrosc. Radiat. Transf.*, *113*(18), 2601–2607, doi:10.1016/j.jqsrt.2012.03.020.

Lane, A. P., and W. M. Irvine (1973), Monochromatic phase curves and albedos for the lunar disk, *Astron. J.*, *78*, 267–277.

Lucey, P. G., and M. A. Riner (2011), The optical effects of small iron particles that darken but do not

redden: Evidence of intense space weathering on Mercury, *Icarus*, *212*(2), 451–462, doi:10.1016/j.icarus.2011.01.022.

Murchie, S. L. et al. (2015), Orbital multispectral mapping of Mercury with the MESSENGER Mercury Dual Imaging System: Evidence for the origins of plains units and low-reflectance material, *Icarus*, *254*, 287–305, doi:10.1016/j.icarus.2015.03.027.

Nittler, L. R. et al. (2011), The major-element composition of Mercury's surface from MESSENGER X-ray spectrometry, *Science*, *333*(6051), 1847–50, doi:10.1126/science.1211567.

Parman, S. W., E. M. Parmentier, and S. Wang (2016), Crystallization of Mercury's sulfur-rich magma ocean, *Lunar Planet. Sci. Conf.*, *47*, 2990.

Peplowski, P. N., R. L. Klima, D. J. Lawrence, C. M. Ernst, B. W. Denevi, E. A. Frank, J. O. Goldsten, S. L. Murchie, L. R. Nittler, and S. C. Solomon (2016), Remote sensing evidence for an ancient carbon-bearing crust on Mercury, *Nat. Geosci.*, (March), doi:10.1038/ngeo2669.

Riner, M. A., and P. G. Lucey (2012), Spectral effects of space weathering on Mercury: The role of composition and environment, *Geophys. Res. Lett.*, *39*, L12201, doi:10.1029/2012GL052065.

Rivera-Valentin, E. G., and A. C. Barr (2014), Impact-induced compositional variations on Mercury, *Earth Planet. Sci. Lett.*, *391*, 234–242, doi:10.1016/j.epsl.2014.02.003.

Robinson, M. S. et al. (2008), Reflectance and color variations on Mercury: regolith processes and compositional heterogeneity., *Science*, *321*(5885), 66–9, doi:10.1126/science.1160080.

Sanchez, J. A., V. Reddy, A. Nathues, E. A. Cloutis, P. Mann, and H. Hiesinger (2012), Phase reddening on near-Earth asteroids: Implications for mineralogical analysis, space weathering and taxonomic classification, *Icarus*, *220*(1), 36–50, doi:10.1016/j.icarus.2012.04.008.

Schlemm, C. E. et al. (2007), The X-Ray Spectrometer on the MESSENGER Spacecraft, *Space Sci. Rev.*, *131*(1-4), 393–415, doi:10.1007/s11214-007-9248-5.

Shkuratov, Y., V. Kaydash, and G. Videen (2012), The lunar crater Giordano Bruno as seen with optical roughness imagery, *Icarus*, *218*(1), 525–533, doi:10.1016/j.icarus.2011.12.023.

Solomon, S. C., R. L. McNutt, R. E. Gold, and D. L. Domingue (2007), MESSENGER Mission Overview, *Space Sci. Rev.*, *131*(1-4), 3–39, doi:10.1007/s11214-007-9247-6.

Thomas, R. J., D. A. Rothery, S. J. Conway, and M. Anand (2014), Hollows on Mercury: Materials and mechanisms involved in their formation, *Icarus*, *229*, 221–235, doi:10.1016/j.icarus.2013.11.018.

Vaughan, W. M., J. Helbert, D. T. Blewett, J. W. Head, S. L. Murchie, K. Gwinner, T. J. McCoy, and S. C. Solomon (2012), Hollow-Forming Layers in Impact Craters on Mercury: Massive Sulfide or Chloride Deposits Formed by Impact Melt Differentiation?, *Lunar Planet. Sci. Conf.*, *43*, 1187.

Vilas, F. (1985), Mercury: Absence of crystalline Fe2+ in the regolith, *Icarus*, *64*(1), 133–138, doi:10.1016/0019-1035(85)90044-2.

Vilas, F. et al. (2016), Mineralogical indicators of Mercury's hollows composition in MESSENGER color observations, *Geophys. Res. Lett.*, doi:10.1002/2015GL067515.

Warell, J. (2003), Properties of the Hermean regolith: III. Disk-resolved vis-NIR reflectance spectra and implications for the abundance of iron, *Icarus*, *161*(2), 199–222, doi:10.1016/S0019-1035(02)00055-6.

Weider, S. Z. et al. (2015), Evidence for geochemical terranes on Mercury: Global mapping of major elements with MESSENGER's X-Ray Spectrometer, *Earth Planet. Sci. Lett.*, *416*, 109–120, doi:10.1016/j.epsl.2015.01.023.

Whitten, J. L., J. W. Head, B. W. Denevi, and S. C. Solomon (2014), Intercrater plains on Mercury: Insights into unit definition, characterization, and origin from MESSENGER datasets, *Icarus*, *241*, 97–113, doi:10.1016/j.icarus.2014.06.013.

Figure captions

Figure 1 (1.5 column)

Variation in visible (VISr) and UV (UVr) spectral slope in different surface units. A steeper visible spectral slope results from greater reflectance at the red end of the spectrum than at the blue end. All spectra from Mercury are 'red–sloped' in this way, but some, such as BCFDs and LRM, are relatively 'blue–sloped' (the spectral slope is flatter). Dashed black lines indicate wavelengths between which ratios are calculated. Sample data are MASCS observations for Eminescu crater, ORB_11217_205406 spectra 1266, 1267 and 1270.

Figure 2 (single column)

High resolution MDIS NAC image EN0221282722M (25 m/pixel) shows that flat hollow floors in Eminescu crater (black arrows) have reflectance comparable to that of the surrounding unhollowed unit, while upstanding knobs of material within hollows (white arrows) and the surrounding BCFD halo have relatively high reflectance. Solar illumination from the left. Highly reflective regions on steep topography result from illumination geometry and do not necessarily indicate high albedo. Centered at 114.4° E, 10.4° N.

Figure 3 (1.5 column)

Comparison of WAC (left, EW0210807816G, 311 m/pixel) and NAC (right, EN0258515991M, 28 m/pixel) images at location 8001 (centered at -33.4°E, 30.5°N), showing how higher–resolution coregistered NAC data provide morphological evidence for the unit type being probed at specific locations on the WAC image.

Figure 4 (1.5 column)

Comparison of the spectral character of hollow floors and surrounding units. Hollow floors reach the highest VISr (lowest spectral slope), whereas BCFD halos and partially-developed hollows reach the highest reflectance. Markers indicate the mean value within a sample area, bars extend to the minimum and maximum pixel values.

Figure 5 (1.5 column)

The MDIS-derived spectral character of hollows in Eminescu crater. (a) Reflectance at 750 nm (EW0249411920G). White outline: extent of (c). Markers indicate central points of MASCS footprints from tracks referred to in the text as Eminescu 1 (yellow dots, ORB_11217_205406), Eminescu 2 (white squares, OB2_12356_152908) and Eminescu 3 (white triangles, ORB_11218_205528). (b) Spectral slope at visible wavelengths (VISr, EW0249411904F/ EW0249411920G). (c) NAC image EN0261857858M with yellow polygons indicating the approximate location of Eminescu 1 footprints plotted in Figure 8a. Base image lighting conditions do not indicate those at the time of the MASCS observations.

Figure 6 (1.5 column)

Variation in phase ratio R(α1)/R(α2) (α1 > α2) in units associated with hollows in Kertesz crater. (a) Image EN1015195239M, high (90°) phase angle. (b) Image EN1012860017M, moderate (36°) phase angle. (c) Ratio image dividing values in (a) by those in (b). Cross-hatching: no data. Hollow

floors have a lower phase ratio than unhollowed crater floor, whereas BCFDs have a higher phase ratio than unhollowed crater floor.

Figure 7 (2 column)

MDIS reflectance spectra from type examples of hollow–related and surrounding units in Raditladi basin, as indicated in Figure SF1. Right column shows values in the left column normalized to the average spectrum of three points on the non–LRM crater floor.

Figure 8 (1.5 column)

The relation between UVr and visible spectral slope (top) and reflectance at 750 nm (bottom) within three MASCS tracks crossing hollow–related units in Eminescu crater. Unit types are attributed on the basis of the unit overlain when plotted on the global monochrome mosaic v9, and R750 and VISr signatures deemed to be characteristic of each unit type on the basis of MDIS data. MASCS footprint locations indicated in Figure 5a. (a) Eminescu 1, ORB_11217_205406, (b) Eminescu 2, OB2_12356_152908, (c) Eminescu 3, ORB_11218_205528.

Figure 9 (1.5 column)

The relation between UVr and visible spectral slope (top) and reflectance at 750 nm (bottom) within three MASCS tracks crossing hollow–related units in Raditladi basin. Unit types are attributed on the basis of the unit overlain when plotted on the global monochrome mosaic v9, and R750 and VISr signatures deemed to be characteristic of each unit type on the basis of MDIS data. MASCS footprint locations indicated in Figure 10a. (a) Raditladi 1, OB4_14173_114353 , (b) Raditladi 2, OB4_14175_034017 , (c) Raditladi 3, ORB_11193_023847.

Figure 10 (1 column)

Locations of MASCS footprints analyzed for Raditladi basin. (a) The hollowed peak ring of Raditladi. White rectangle indicates the extent of (b). Markers indicate central points of MASCS footprints from tracks referred to in the text as Raditladi 1 (yellow dots, OB4_14173_114353), Raditladi 2 (white squares, OB4_14175_034017) and Raditladi 3 (white triangles, ORB_11193_023847) (excerpt from global monochrome mosaic, v9). (b) Raditladi 1 MASCS footprints crossing hollows (outlined in yellow), the spectral metrics of which are plotted in Figure 9a. Base image: NAC EN1015483484M georeferenced to the global monochrome mosaic (taken at a different time and so under different lighting conditions than the MASCS observations).

Supplementary Material captions

Figure SF1 Sites featuring flat-floored hollows. Headings correspond to the catalogue number of the hollow group. Outlines indicate the extent of samples within which minimum, maximum and mean values are plotted in Figure 4. Base: WAC images through the 750 nm filter.

Figure SF2 The relation between UVr and visible spectral slope (top) and reflectance at 750 nm (bottom) for hollow-related units as listed in Table ST2, with Raditladi 1 and 2 and Eminescu 1 excluded.

Figure SF3 Variability in the UVr of LRM within hollowed (left) and non-hollowed (right) sites. MASCS observation numbers are listed in Table ST2.

Table ST1 Hollow group locations identified on MESSENGER data released to March, 2015, including those published in *Thomas et al.* [2014].

Table ST2 MASCS observations of hollows and LRM locations used in this analysis.

Tables

Table 1. Sites used to analyze the spectral character of hollow floors. Group ID is the catalogue number in *Thomas et al.* [2014]. Substrates: High–reflectance plains (HRP), Intermediate Terrain (IT), Low–Reflectance Blue Plains (LBP), Low–Reflectance Material (LRM) and Bright ejecta (BE).

Group ID	Latitude (°N)	Longitude (°E)	Regional substrate	Local substrate	Crater name	Multispectral image resolution (m/px)	Multispectral image phase angle (°)
4030	38.5	175.6	HRP	LRM	Balanchine	188	37
5001	7.7	33.2	IT	LRM	Seuss	415	28
6001	46.1	134.8	IT	LRM	Pasch	167	48
6040	41.3	123.9	LBP	LRM		185	46
6054	10.7	114.4	IT	LRM	Eminescu	410	31
6055	27.4	119.1	IT	LRM,HRP	Raditladi	338	39
6070	27.3	146.1	HRP	LRM,BE	Kertesz	271	28
7020	40.4	-138.1	HRP	LRM		188	57
8001	30.5	-33.4	IT	LRM		311	31
8006	50.8	-39.7	IT	BE		216	52

Table 2. Unit types associated with hollows

Unit type	**Description**
Hollow floor	Flat hollow floor
BCFD halo	An area of diffuse high–reflectance material at the margin of a hollow
Partially–developed hollows	An area where sub–pixel–scale hollows and upstanding knobs are seemingly draped by diffuse high–reflectance material (e.g. white arrows in Figure 2)
LRM	Low–reflectance surfaces outside hollows
Crater wall/floor	Crater materials that are not clearly LRM on the basis of R750

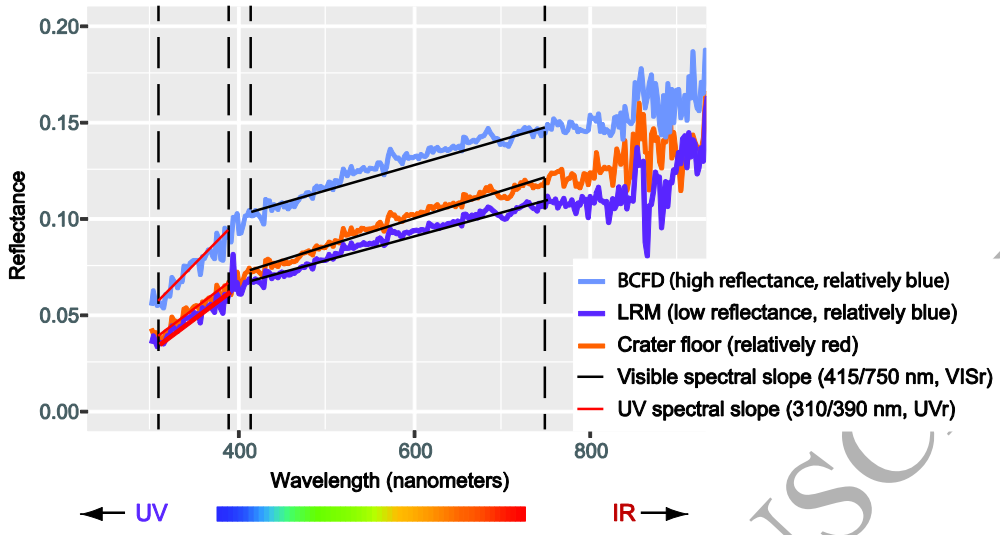

Fig. 1

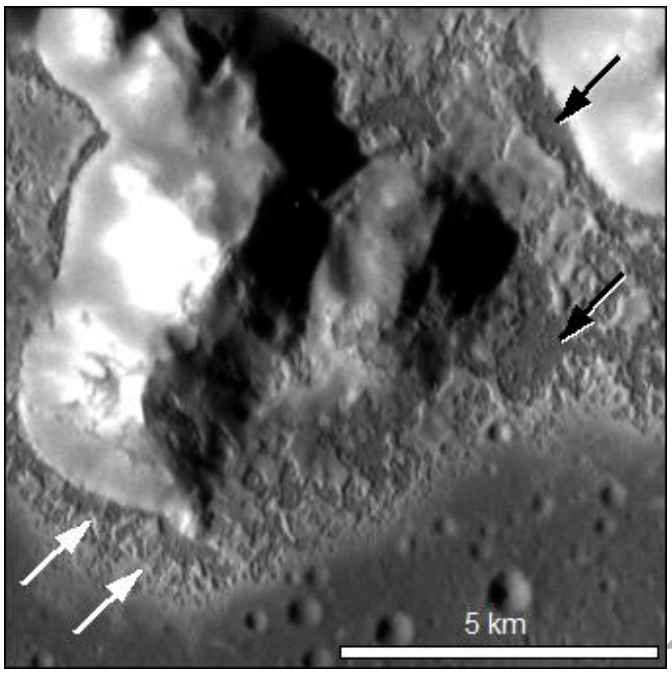

Fig. 2

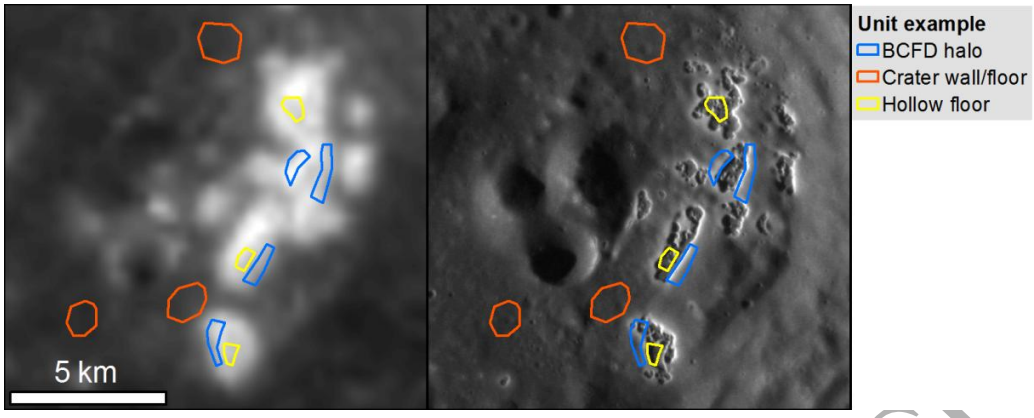

Fig. 3

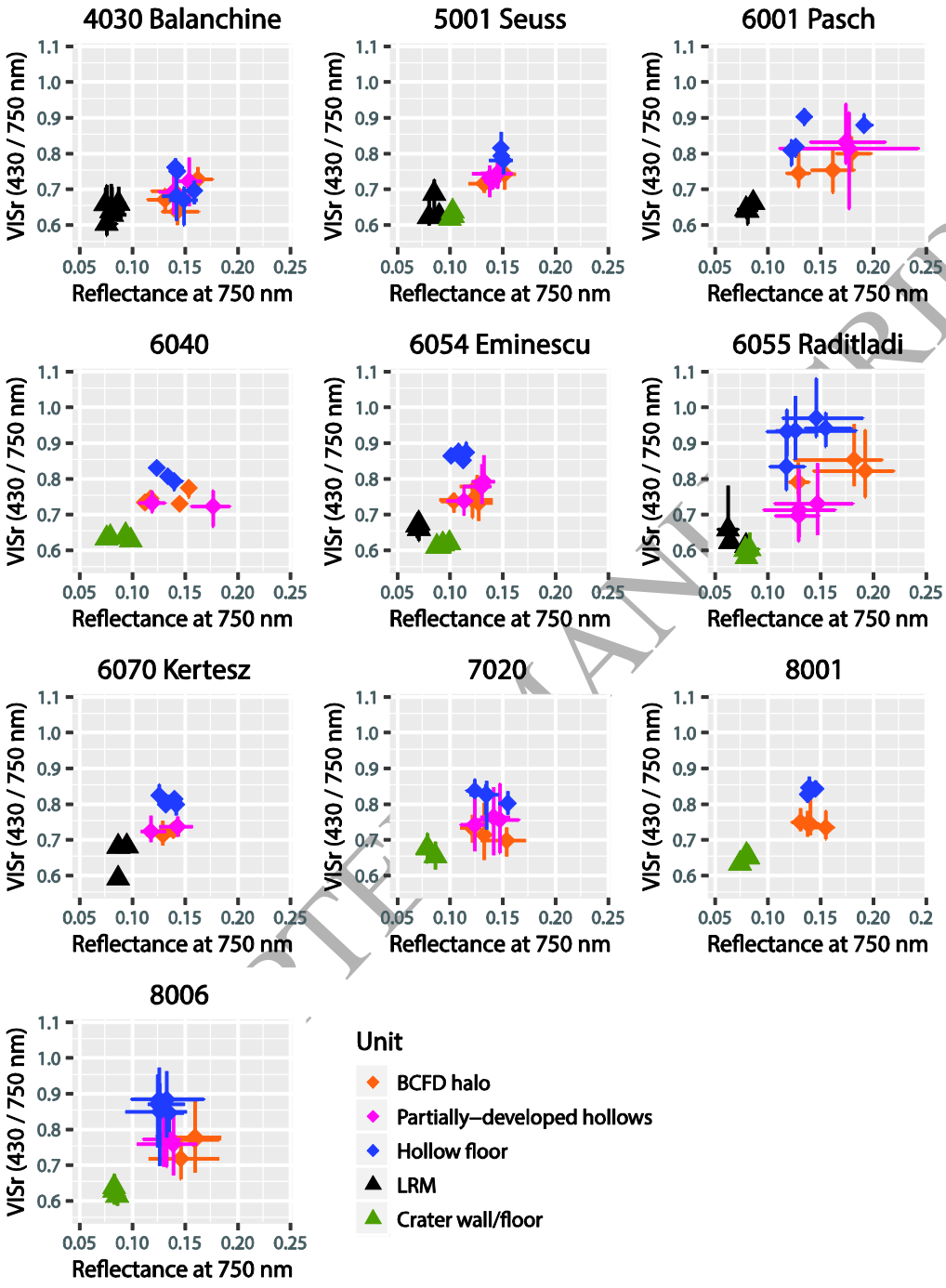
4030 Balanchine
5001 Seuss
6001 Pasch
6040
6054 Eminescu
6055 Raditladi
6070 Kertesz
7020
8001
8006
VISr (430 / 750 nm)
Reflectance at 750 nm
Unit
BCFD halo
Partially–developed hollows
Hollow floor
LRM
Crater wall/floor

Fig. 4

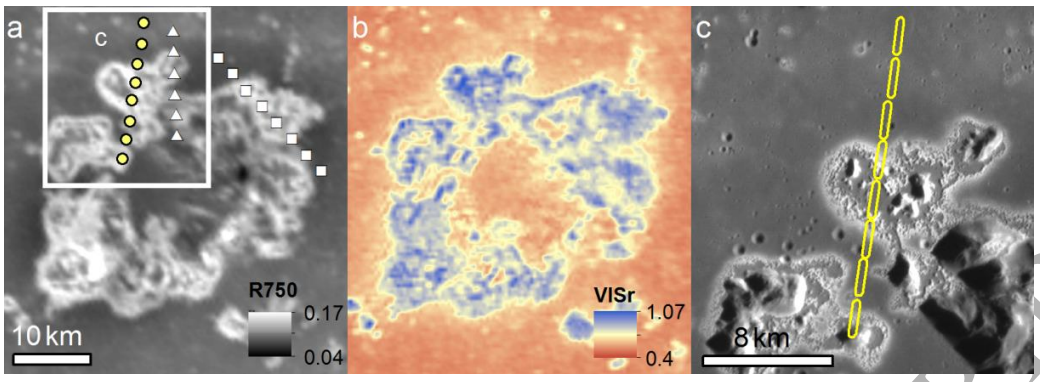

Fig. 5

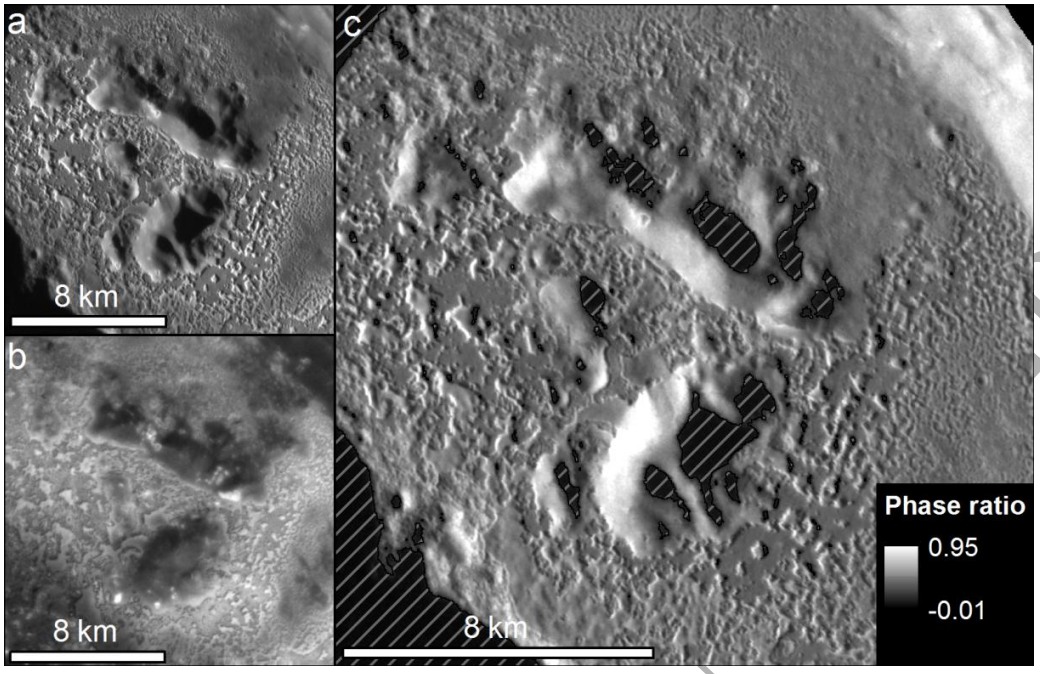

Fig. 6

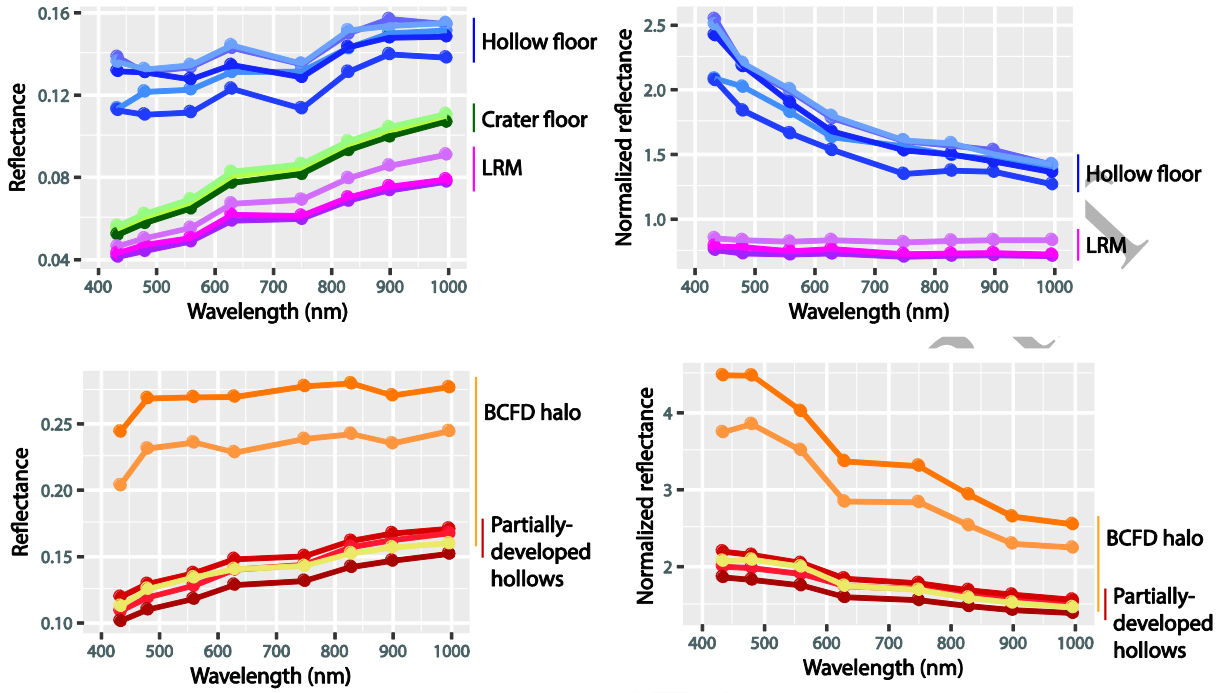

Fig. 7

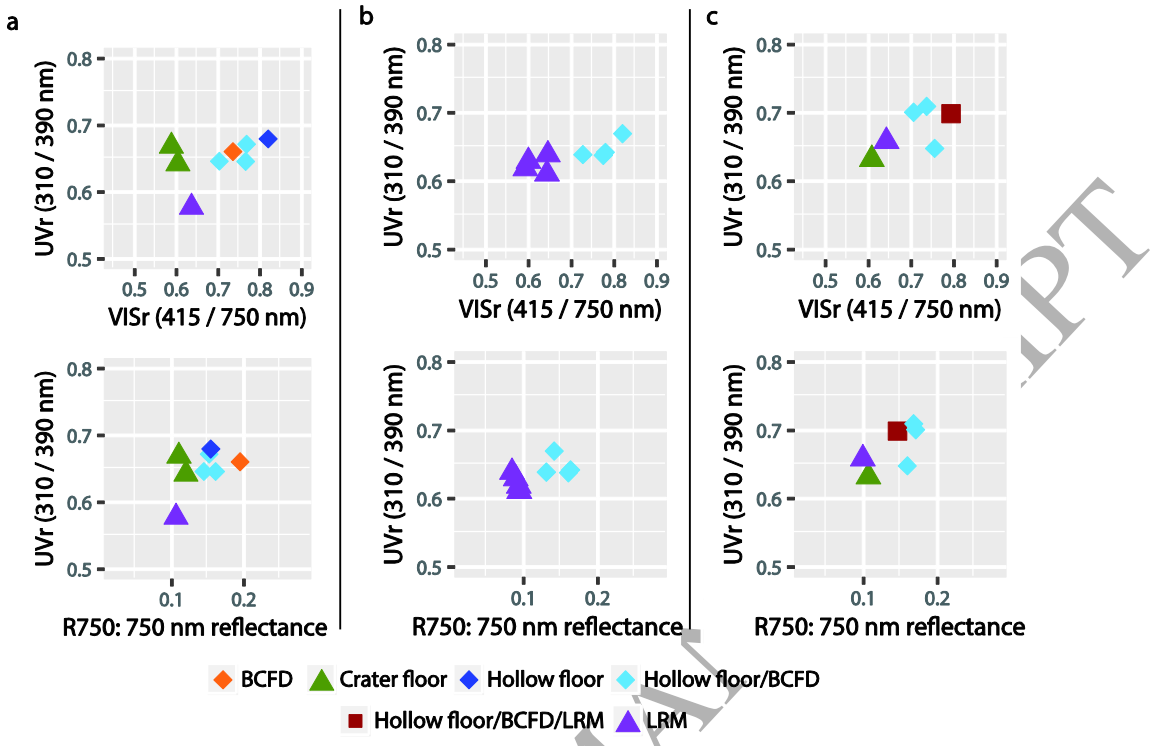

Fig. 8

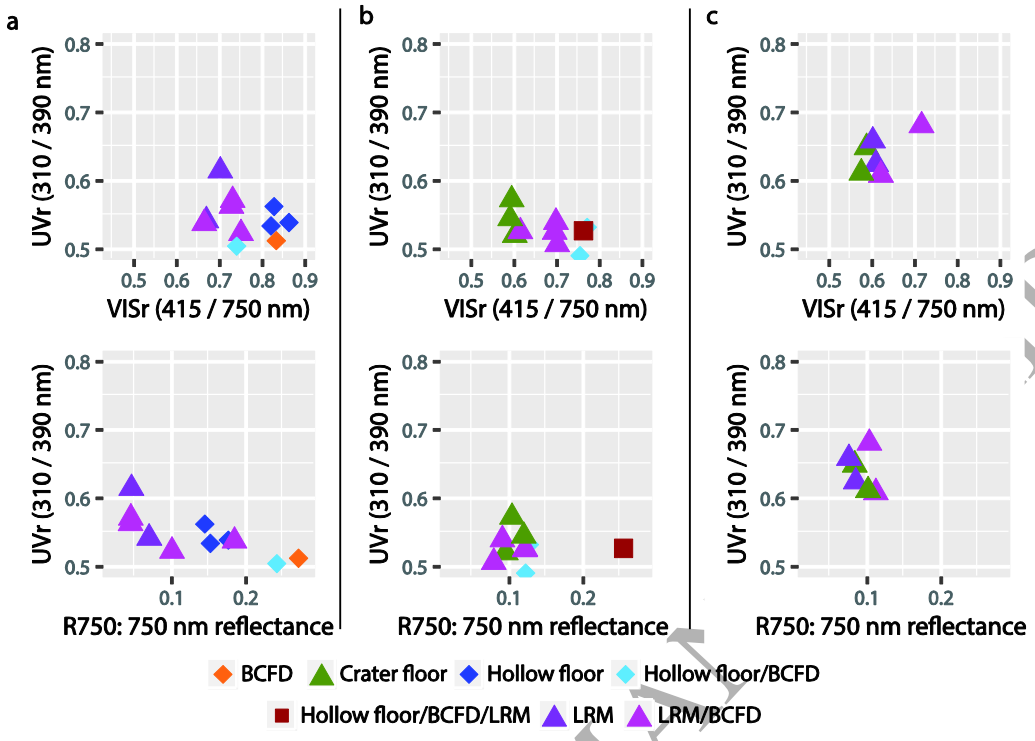

Fig. 9

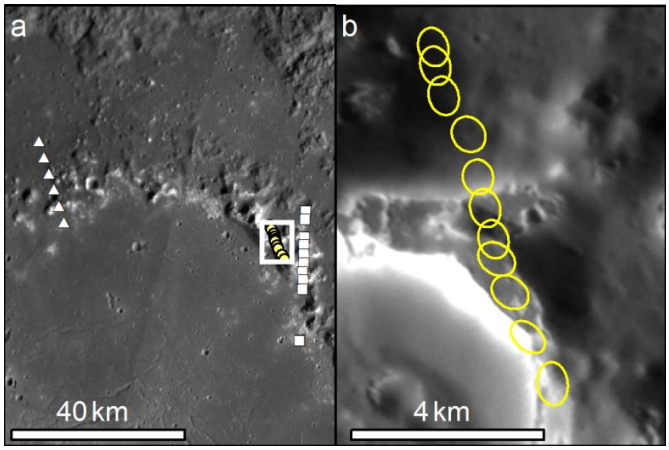

Fig. 10